


Article

Experimental and Numerical Analysis of Flexural Properties and Mesoscopic Failure Mechanism of Single-Shell Lining Concrete

Jian Wu ¹, Haijun Zou ¹, Nengfang He ¹, Haiyan Xu ², Zhijie Wang ³ and Xiaohao Rui ^{3,*} 

¹ Road & Bridge South China Engineering Co., Ltd., Zhongshan 528405, China; wujian0404@163.com (J.W.); henengfang0722@163.com (N.H.)

² School of Civil Engineering, Sichuan Agricultural University, Chengdu 611830, China; zouhaijun1288@163.com (H.Z.); haiyanxu@sicau.edu.cn (H.X.)

³ School of Civil Engineering, Southwest Jiaotong University, Chengdu 610031, China; zhjiwang@home.swjtu.edu.cn

* Correspondence: xiaohao97@my.swjtu.edu.cn



Citation: Wu, J.; Zou, H.; He, N.; Xu, H.; Wang, Z.; Rui, X. Experimental and Numerical Analysis of Flexural Properties and Mesoscopic Failure Mechanism of Single-Shell Lining Concrete. *Buildings* **2024**, *14*, 2620. <https://doi.org/10.3390/buildings14092620>

Academic Editor: Mizan Ahmed

Received: 26 July 2024

Revised: 14 August 2024

Accepted: 15 August 2024

Published: 24 August 2024

Correction Statement: This article has been republished with a minor change. The change does not affect the scientific content of the article and further details are available within the backmatter of the website version of this article.



Copyright: © 2024 by the authors. Licensee MDPI, Basel, Switzerland. This article is an open access article distributed under the terms and conditions of the Creative Commons Attribution (CC BY) license (<https://creativecommons.org/licenses/by/4.0/>).

Abstract: Despite ongoing research efforts aimed at understanding the structural response of steel fiber reinforced concrete (SFRC), there is very limited research on the failure characteristics and mesoscopic damage mechanism of SFRC, specifically when under flexure. In this study, a four-point bending test of plain concrete (PC) and SFRC with different fiber contents is carried out to investigate the flexural performance of SFRC. The crack propagation process, cracking load, ultimate load, and load-deflection curves of PC and SFRC beams are obtained. Additionally, the discrete element method (DEM), using PFC2D 6.0 software, is adopted to explore the mesoscopic properties of PC and SFRC. The test and simulation results of PC and SFRC beams are compared and analyzed, and some conclusions are drawn. The results show that steel fiber can efficiently improve the compressive strength of concrete when the fiber content is 30 kg/m³, and significantly improve the deformation resistance, crack resistance, and flexural capacity of concrete. The refined numerical models of PC and SFRC beams are established based on compressive strength and aggregate screening results. Through the numerical four-point bending test, the mesoscopic mechanical behaviors of models reveal the damage mechanism of SFRC. The horizontally distributed steel fibers bridge both sides of the cracks to resist crack development, and the vertically distributed steel fibers guide the cracks to the place with strong contact, thus resisting crack height development. The test results show that, for flexural properties, the optimal steel fiber content of SFRC is 31 kg/m³.

Keywords: steel fiber reinforced concrete; discrete element modeling; failure mechanism; flexural properties; mesoscopic mechanical behaviors

1. Introduction

Concrete is a widely used traditional building material, but the mechanical properties of ordinary concrete gradually begin to fail to meet the needs of some areas. Fibers can effectively improve the tensile strength, crack resistance, energy absorption capacity, and the flexural toughness of the structure [1–4]. The reinforcing effect of fibers on the mechanical properties of concrete is generally related to the shape, size, content, and physicochemical properties of the fibers used [5]. The fibers used in concrete, with regard to their materials, are divided into four basic groups: steel, glass, synthetic, and natural fibers [6]. A review of past studies indicated that the addition of steel fibers into concrete can effectively improve the modulus of rupture and the splitting tensile strength [7], the energy absorption and load-carrying capability [8,9], shear capacities, deformation capacities and stiffnesses [10], and the compressive strength [11].

Some research has been carried out by previous researchers on the properties of steel fiber reinforced concrete. Doyon-Barbant and Charron [12] investigated the effects of fiber distribution direction and density on the tensile, bending, and shear properties

of concrete, and the results showed that the tensile and bending properties of concrete are mainly influenced by the fiber distribution direction, while the shear properties are mainly influenced by the fiber density. Varona et al. [13] conducted a study on the bond strength of steel reinforcement of concrete in high-temperature environments, and tested the bond strength of concrete at high and ambient temperatures by performing pull-out tests on fiber reinforced concrete, which showed that steel fibers with a high aspect ratio are beneficial to the bond strength of concrete in high-temperature environments. Furthermore, Chu and Kwan developed a new bond model of SFRC by modifying the existing one for plain concrete in Model Code 2010 with a finite initial bond stiffness. They found that concrete strength and steel fibers have a synergistic effect on the bond performance of SFRC [14]. Meanwhile, the addition of steel fibers can enhance the mechanical and thermal behavior of concrete at high temperatures [15]. Awolusi et al. [16] found that the fresh and hardened properties of SFRC can be predicted using response surface methodology (RSM), which uses aspect ratio, water cement ratio, and cement content as independent variables. They finally obtained prediction equations for the water absorption, compressive strength, flexural strength, splitting tensile strength, and slump of SFRC.

Among the mechanical properties of concrete, the flexural properties are crucial [17]. The flexural mechanical behavior of SFRC has recently attracted the attention of a large number of researchers. Magureanu et al. [18] conducted an experimental study on the flexural properties of SFRC beams and showed that steel fibers have a significant effect on the tensile strength of concrete beams, and that the ductility and load-carrying capacity of the beams are increased significantly compared to plain concrete (PC) beams. Similar conclusions have been reached by other researchers [19–21]. Khalil and Tayfur [22] conducted some studies on the flexural load-carrying capacity of SFRC beams. They tested 11 SFRC beams with different fiber contents and shapes. The results showed that the steel fibers had a significant effect on the flexural load-carrying capacity of the specimens, with a 27% and 23% increase in flexural load-carrying capacity for wave-shaped steel fibers and curved hook-shaped steel fibers, respectively, when the fiber volume fraction was 1%. Yang et al. [23] conducted a comparative analysis of the flexural performance and reasonable design specifications of SFRC. It was found that the distribution and direction of fibers were influenced by the method of concrete placement.

To date, a number of studies have been carried out to explore the flexural performance of SFRC by conducting an indoor bending test. However, more and more researchers have started to investigate the bending behavior of SFRC through numerical simulation. Numerical simulation has a higher loading accuracy compared with the indoor test, and can save a lot of labor and material resources with good economic applicability. The test is repeatable so that the test phenomenon can be repeatedly explored in depth, and the time spent is shorter than on the indoor test. In order to study the effect of steel fiber admixture and length on the load-bearing capacity of concrete beams, Kan et al. [24] simulated the crack expansion process of concrete beams through a four-point bending test, and numerical simulation analysis was performed using the extended finite element method (XFEM) of ABAQUS 2019. The results showed that the flexural performance of concrete improved with the increase in length and the content of fiber, but that the strengthening effect produced by different contents and lengths of steel fiber was different. Kusumaningrum et al. [25] also performed three-point bending test simulations with reactive powder concrete (RPC) containing steel fibers, using the extended finite element method, and then analyzed the tensile stress, CMOD, and fracture energy; the simulation results obtained were in good agreement with the experimental results. Soetens et al. [26] proposed a method to characterize the nonlinear bending properties of steel fiber concrete by performing the finite element (FE) analysis on a prism model, and the model obtained correlated well with the experimental results. This literature review reveals that there are available numerical models for SFRC, which are mostly based on continuum theory. However, the micro and meso structure of concrete is hard to represent as a continuum, since there are a large number of voids, varying sized aggregates, and other heterogeneities [27–29]. Due to the

non-uniformity of concrete structures, loads are transferred through discrete load paths. Therefore, the use of a discrete element numerical simulation can better reflect the load transfer and deformation process of concrete, and especially its microscopic mechanical properties, compared to a finite element analysis [30].

In this paper, the influence of steel fiber on the crack resistance and flexural performance of single-shell lining concrete is investigated. With the same curing conditions, the mechanical properties of single-shell lining concrete are evaluated through measurement of its compressive strength, cracking load, ultimate load, and flexibility. To the authors' knowledge, few research studies have been performed which use the discrete element method to explore the mesoscopic flexural properties of SFRC. A new method for the discrete modelling of SFRC is presented, which provides a possibility for investigating the failure properties and mesoscopic damage mechanism of concrete. In the section regarding numerical investigations, the numerical four-point bending test is compared with the experimental results. In addition, the compressive strength, cracking load, ultimate load, and flexibility of SFRC with different fiber contents are predicted.

2. Experimental Programs

2.1. Materials and Proportions

The SFRC in the experiment was made from the following components: fly ash, fine aggregate, coarse aggregate, water reducer, water, PO42.5 grade ordinary Portland cement, and steel fiber. Coarse aggregate here refers to aggregate with a nominal particle size of 5~20 mm and good gradation, while fine aggregate refers to river sand with a fine modulus of 2.5 and good gradation. The steel fiber used in this study was Dramix 4D 80/60 BG, with a diameter of 0.75 mm and a length of 60 mm (see Figure 1a). Twenty-four concrete beam specimens were made, including six PC beam specimens without steel fiber (PC0-1~6) and eighteen SFRC beam specimens with 20 kg/m³ (SFRC20-1~6), 30 kg/m³ (SFRC30-1~6), and 40 kg/m³ (SFRC40-1~6), respectively (see Table 1). For a better explanation, the mix proportions of the concrete are shown in Table 1.

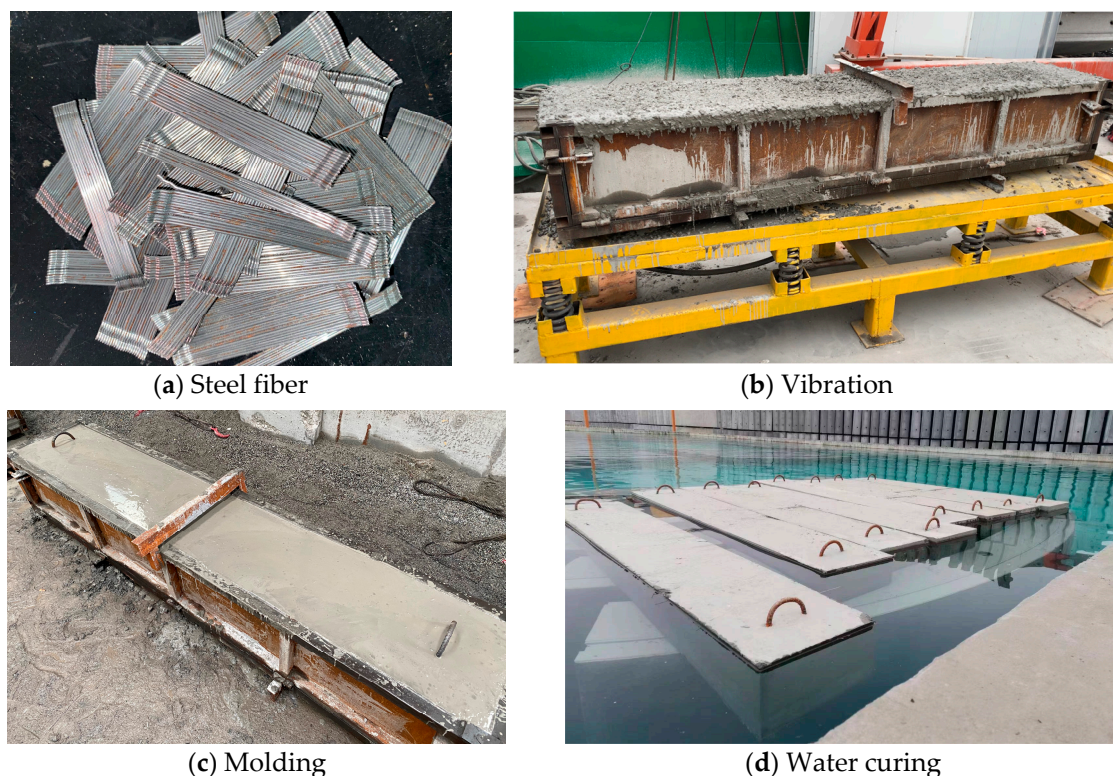


Figure 1. The casting and curing process of a specimen.

Table 1. The mix proportions of PC and SFRC with different fiber contents.

Specimens	Steel Fiber/ kg	Fly Ash/ kg	Fine Aggregate/ kg	Coarse Aggregate/kg		Water Reducer/ kg	Water/ kg	Cement/ kg
				5.0~10.0/ mm	10.0~20.0/ mm			
PC0-1~6	0	60	796	100	1095	3.96	135	380
SFRC20-1~6	20	60	796	100	1095	4.26	135	380
SFRC30-1~6	30	60	796	100	1095	4.56	135	380
SFRC40-1~6	40	60	796	100	1095	4.86	135	380

2.2. Fabrication of Specimens and Loading Method

Under actual stress conditions, single-shell lining concrete can be analyzed using beam structures. The fibers, gravel, and sand were firstly put into the blender at the same time and stirred for 20 s, then they were mixed with water and stirred for 20 s, then they were mixed with cement and admixtures for 90~100 s, and finally the water reducer was added and stirred for 30 s. The stirring time of SFRC was 20~30 s longer than that of PC, and the agglomeration of steel fiber was avoided during stirring. According to the Chinese code CECS 13:2009 Standard test methods for fiber reinforced concrete, the mixed concrete was loaded into the mold in one go and to a level slightly higher than the top of the mold. Then, it was placed on the vibration table to vibrate for 60 s (see Figure 1b). Excess concrete was scraped off, and the specimens were finally flattened (see Figure 1c). The specimens were numbered and left in the laboratory for one day, after which the molds were removed, and the specimens were placed in a standard curing pond for 28 curing days (see Figure 1d).

2.2.1. Rebound Strength Test

In order to obtain the compressive strength of straight beam members, rebound strength tests were conducted on PC and SFRC beams with different fiber contents. According to the requirement of the Chinese code JGJ/T 23-2011 Technical specification for inspection of concrete compressive strength by rebound method, four straight beams were randomly selected from the same batch of specimens for inspection. For each specimen, the number of rebound measurement areas cannot be fewer than 10. In each measurement area, 16 rebound values were read, 3 maximum values and 3 minimum values were excluded from the 16 values, and the remaining 10 rebound values were calculated according to Equation (1).

$$R_m = \frac{\sum_{i=1}^{10} R_i}{10} \quad (1)$$

where R_m is the average rebound value (MPa) in the survey area, and R_i is the rebound value (MPa) of the i th measuring point. The rebound strength R_m is converted to the concrete conversion strength f_{cu} (MPa) in the measurement area according to the conversion table, which is used as the compressive strength of the specimen.

2.2.2. Pure Bending Test

To explore the bending performance of steel fiber reinforced concrete, the four-point bending test was carried out. The size of the bending test specimen was $2400 \times 400 \times 350$ mm. The specimens were divided into four groups, corresponding to PC and SFRC beams with different fiber contents. The loading devices of the test are shown in Figure 2.

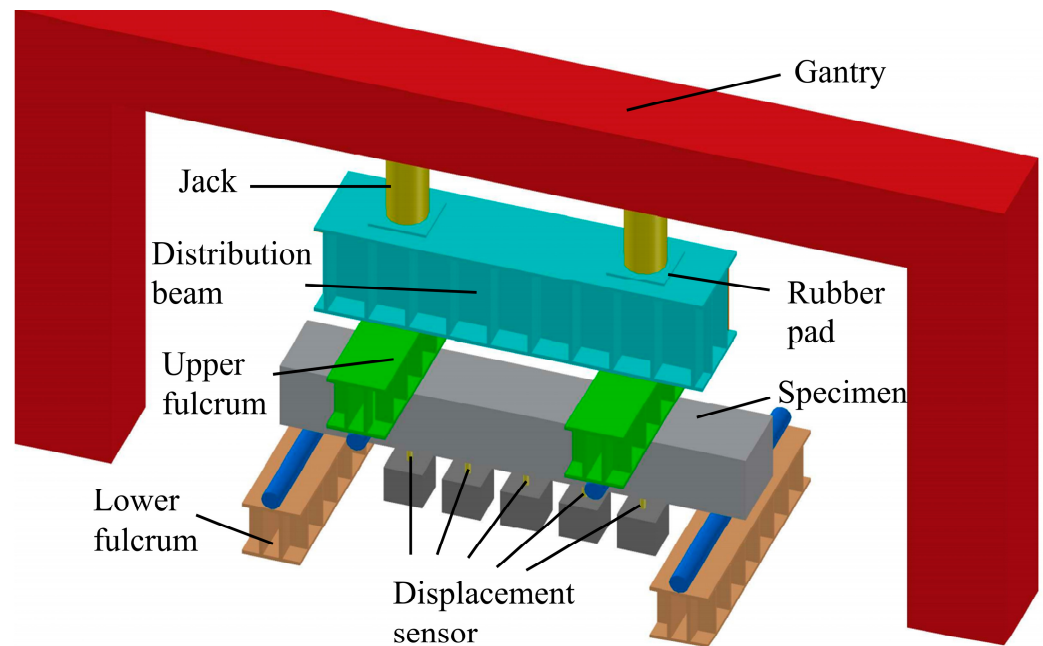


Figure 2. Loading equipment for the four-point bending test.

The loading devices were two hydraulic jacks with a maximum loading capacity of 400 kN (see Figure 2). The force provided by the jack is transferred to two points of the specimen through the distribution beam, whose capacity is 1200 kN. The measure devices include the pressure transducer, which measures the force produced by the hydraulic jack, the strain gauge attached to the specimen with its automatic data acquisition system, and the displacement sensor placed at the bottom of the specimen, which records the deflection (see Table 2).

Table 2. Technical requirements for instruments for the bearing capacity performance test.

Name	Unit	Technical Indicators		
		Range	Graduation Value	Accuracy
Pressure sensor	kN	1000 and 2000	0.1	Level 1
Crack microscope	mm	10	0.01	0.01
Displacement gauge	mm	30	0.01	Level 1
Electronic stopwatch	s	>2 h	1 s	
Hydraulic jack	kN	400	Ensure continuous or staged pressurization or decompression	
Loading system control box		Connect all pressure sensors and displacement gauges		
Receiving system of load and displacement		Manually or automatically record the pressure, displacement, and other data of each loading stage		

During the test, the load increment of each level should be small. Record the load when the crack width of the PC specimen reaches 0.2 mm, and then continue to load until the crack width of the PC specimen reaches 2.5 mm. Then, the test shall be terminated after loading 1–2 levels, or immediately terminated according to the situation. After that, the four-point bending test of the SFRC specimen should be carried out. Based on the load, when the crack width of the PC specimen reaches 0.2 mm and 2.5 mm, it is loaded by stages. When it is close to the load before, reduce the speed of loading, and record the crack width of the SFRC in each stage. The test should be terminated under one of the following circumstances:

- (1) The concrete reaches the ultimate compressive strain (crushing) (strain gauges are arranged on the compression zone).

- (2) The maximum crack width at the tension zone reaches or exceeds 2.5 mm.
- (3) The load cannot continue to increase.

3. Results

3.1. The Rebound Strength

According to the method in Section 2.2.1, the converted compressive strengths of PC and SFRC specimens with different fiber contents and the compressive strength enhancement factors of SFRC specimens were calculated (see Figure 3). As shown in Figure 3, the compressive strength of the 20 kg/m³ and 40 kg/m³ SFRC specimens were almost at the same level as PC, and the maximum and minimum compressive strengths in the 20 kg/m³ SFRC specimens were 45.7 MPa and 43.7 MPa, respectively, with an average strength enhancement coefficient of 0.013. The maximum and minimum compressive strengths of the 30 kg/m³ SFRC specimens were 61.0 MPa and 57.0 MPa, respectively, with an average strength enhancement factor of 0.343. The maximum and minimum compressive strengths of 40 kg/m³ SFRC were 45.7 MPa and 42.0 MPa, respectively, with an average strength enhancement coefficient of −0.013. When the fiber content is 20 kg/m³, the effect of steel fiber on the compressive strength of concrete is not significant and, even when the fiber content is 40 kg/m³, the average strength enhancement coefficient is −0.013, indicating that too much steel fiber may have a reducing effect on the compressive strength of concrete. When the fiber content is 30 kg/m³, the compressive strength of SFRC is significantly greater than that of PC and other SFRC specimens, with a maximum strength enhancement coefficient of 0.377, and an average strength enhancement coefficient reaching 0.343.

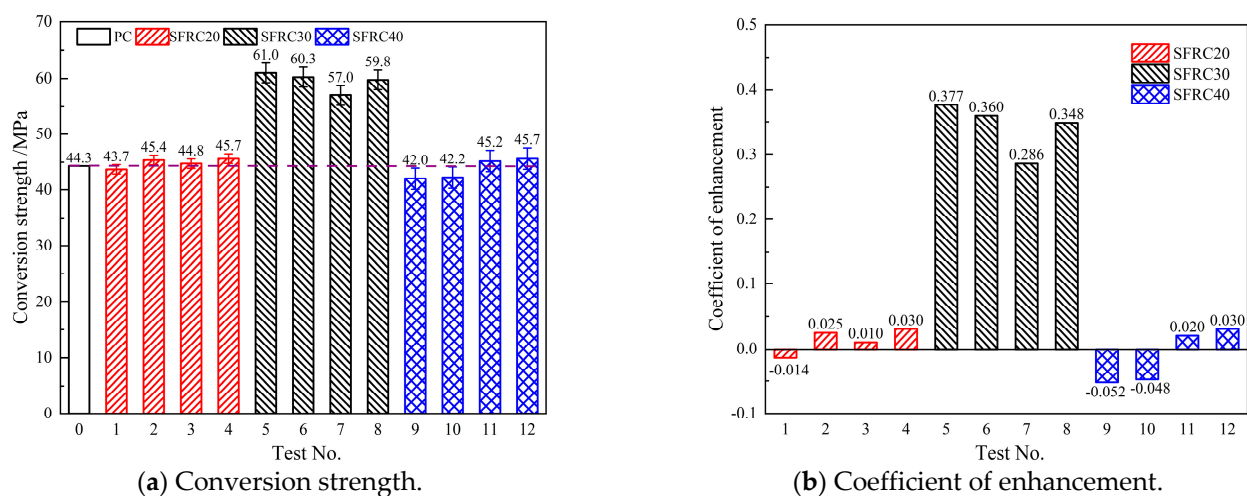


Figure 3. Conversion strength and coefficient of enhancement. (Coefficient of enhancement = [Strength of SFRC (MPa) – Strength of PC (MPa)]/Strength of PC (MPa)).

Further analysis of the converted compressive strengths of the SFRC specimens shows that the SFRC20 and SFRC40 specimens had similar compressive performance, with average compressive strengths of 44.9 MPa and 43.8 MPa, respectively, while the average compressive strength of the SFRC30 specimens reached 59.5 MPa, which is 32.5% and 35.8% higher than that of SFRC20 and SFRC40, respectively. The SFRC40 specimens show the worst performance, and more bubbles also appeared on the surface of the SFRC specimens after vibrating during the casting process. The reason for this may be that, under the low water–cement ratio, the increased amount of steel fiber makes even distribution difficult, and the excessive steel fiber content could cause a greater air content inside the concrete during mixing and forming, resulting in lower compressive strength. The right amount of steel fiber can significantly improve the compressive strength of concrete. Zhang et al. [11] also obtained similar conclusions in their research. Their tests obtained the compressive strength of SFRC with fiber volume fractions of 0%, 0.5%, 0.75%, 1.0%, and 1.5%, and found

that the compressive strength of SFRC reached its maximum at a volume fraction of 0.75%, which was 15.5% higher than that of PC.

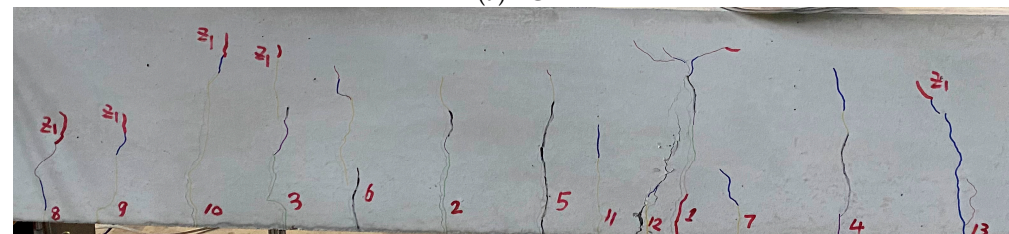
3.2. Results of Four-Point Bending Test

3.2.1. Failure Mode of Specimens

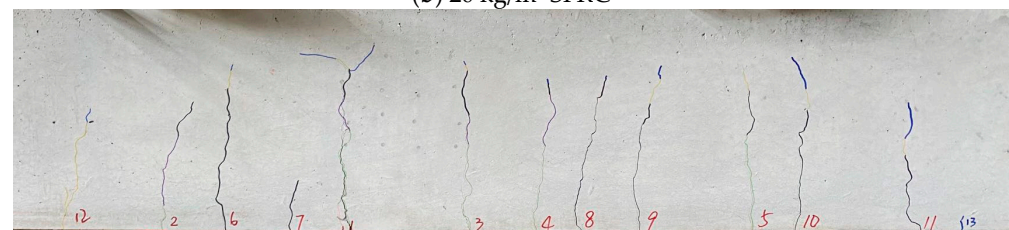
Figure 4 shows pictures of the cracks on the specimens with different fiber contents at the failure stage. Due to the limitation of space, and for the convenience of analysis, PC0-7, SFRC20-1, SFRC30-3, and SFRC40-5, which are representative at each group of specimens, were selected for the investigation of crack development. As is seen in Figure 4a, the cracks on the middle of the PC specimen developed vertically at the beginning, and began to develop diagonally in the later stage of the test. Some of the cracks showed the ‘bifurcation’ phenomenon when they were about to extend to the top of the beam. When the load was 66.03 kN, the initial crack appeared near the loading point (crack No. 7), with a crack width of 0.02 mm and a height of 4 cm. When the load reached 86.08 kN, the maximum crack width was 0.20 mm, reaching the serviceability limit states. At this time, there were two cracks on the surface of the specimen, with the height of 17.0 cm and 22.5 cm, respectively. When the load reached 179.27 kN, the maximum crack width of the specimen reached 2.50 mm, at which time there were 11 cracks on the specimen (see Figure 4a), and the cracks near the two loading points were beginning to extend toward the top of the beam and develop mostly along the oblique direction due to the excessive shear force. In general, there is uniform horizontal spacing between adjacent cracks.



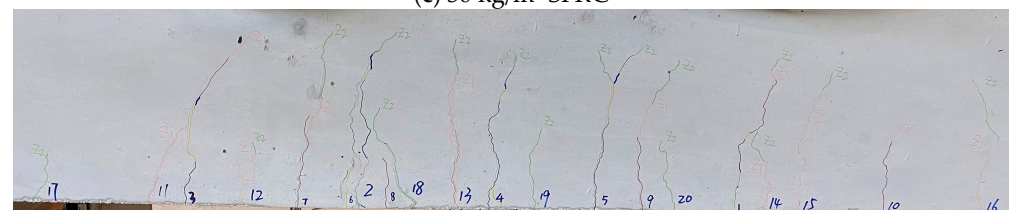
(a) PC



(b) 20 kg/m³ SFRC



(c) 30 kg/m³ SFRC



(d) 40 kg/m³ SFRC

Figure 4. The failure patterns of specimens with different fiber contents.

Figure 4b shows the crack development of the 20 kg/m³ SFRC specimens. The number of cracks is higher than in PC, and the spacing between cracks has no obvious regularity. The initial crack appeared at a load of 83.34 kN near the loading point (crack No. 1), with a crack width of 0.03 mm and a crack height of 8 cm. When the load reached 135.65 kN, the maximum crack width was 0.20 mm, reaching the serviceability limit states. At this time, there were five cracks with a maximum height of 28 cm (crack No. 1). When the load reached 228.54 kN, the maximum crack width reached 2.50 mm, and there were 13 cracks at this time (see Figure 4b). Cracks No. 1 and No. 10, near the two loading points, were about to extend to the top of the beam, and cracks No. 1 and No. 12 had penetrated and developed horizontally along the oblique direction. In general, the development of the cracks was more curved, since steel fiber limits and changes the development path of cracks.

Figure 4c shows the crack development of the 30 kg/m³ SFRC specimens. It can be seen that the number of cracks is also slightly higher than that of PC, but the crack density is higher than that of the 20 kg/m³ SFRC specimen. The initial crack appeared at a load of 96.48 kN near the loading point (crack No. 1), with a crack width of 0.02 mm and an initial height of 1 cm. When the load reached 172.11 kN, the maximum crack width was 0.20 mm, reaching the serviceability limit states. At this time, there were five cracks on the specimen, and the maximum height was 21.5 cm (crack No. 4). When the load reached 267.90 kN, since the vertical deformation speed of the specimen had exceeded the loading speed of the jack, the load was difficult to stabilize and could not continue to increase; the maximum crack width of the specimen reached 2.50 mm, and there were 13 cracks on the specimen (see Figure 4c). The height of crack No. 1 near the loading point extended to 31 cm, and the top of the crack began to develop and bifurcate horizontally. In general, most of the cracks did not extend to the top of the beam and, eventually, the degree of development was lower than that of PC.

Figure 4d shows the crack development of the 40 kg/m³ SFRC specimens. It can be seen that the number of cracks is significantly higher than in plain concrete, and the crack density is also higher than that of PC and the other SFRC specimens. The initial crack appeared at a load of 64.15 kN near the right loading point (crack No.1), with a crack width of 0.01 mm and an initial crack height of 1.5 cm. When the load reached 130.27 kN, the maximum crack width was 0.20 mm, which reached serviceability limit states. At this time, there were five cracks on the specimen, with a maximum height of 25.8 cm (crack No. 2). When the load reached 247.72 kN, the maximum crack width of the specimen was 2.50 mm, there were 21 cracks on the specimen at that time (see Figure 4d), and the height of crack No. 2 near the loading point extended to 29.7 cm; most of the cracks were about to extend toward the top of the beam, and some of the cracks had penetrated. In general, the path of crack development is tortuous and is obviously influenced by steel fibers.

In summary, the cracking load of PC is generally lower than that of SFRC, indicating that steel fibers have a resistant effect on the cracking of concrete, and that the effect varies with the fiber content (see Figure 5). As shown in Figure 5, the cracking and ultimate loads of PC are generally lower than those of SFRC. For the cracking load, the SFRC20, SFRC30, and SFRC40 specimens increased by 34.57%, 90.48%, and 24.87%, respectively, compared with PC. While the ultimate load of the SFRC20, SFRC30, and SFRC40 specimens increased by 28.12%, 47.22%, and 40.59%, respectively. The cracks on the SFRC specimens are subtler, more numerous, and widely distributed. Since the ultimate load of an SFRC specimen is generally higher than that of PC, the surface of an SFRC specimen thus produces more cracks after most of the tension zone of the concrete matrix has ceased working, and the steel fibers near the cracks continue to bear the load. The sound of fiber fragmentation can be heard in the later stage, the surface of the specimen features flaky fragments falling off, and the exposed steel fibers have been deformed, resisting well the development of cracks in the later stages of test. After the end of the test, a certain amount of exposed steel fiber connected both sides of the crack (see Figure 6). It can be seen that steel fiber plays a key role in the crack resistance and toughening of concrete.

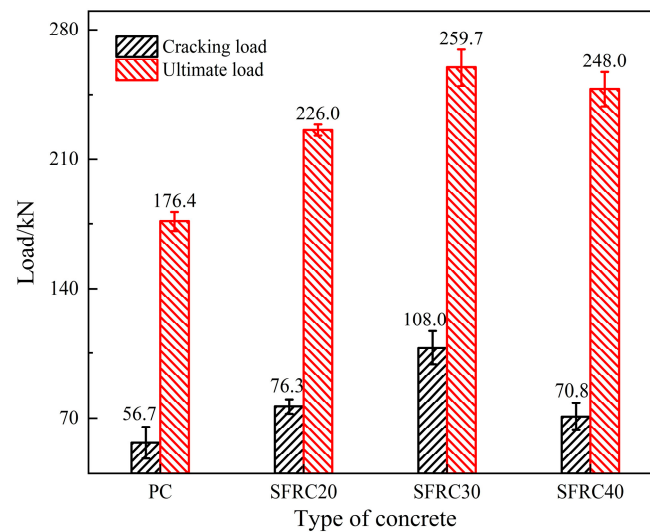


Figure 5. The cracking load and ultimate load of PC and SFRC specimens.

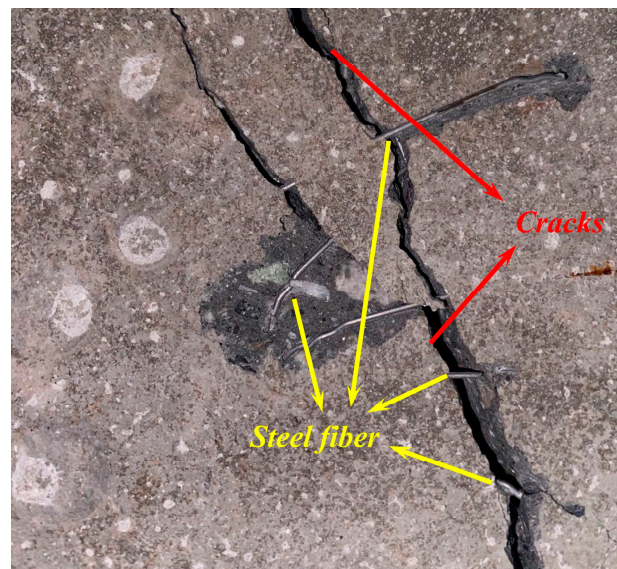


Figure 6. A partial enlarged image of cracks on an SFRC specimen.

3.2.2. The Deflection of Concrete

Five sensors were arranged equidistantly at the bottom of the specimen to monitor the deflection of the concrete during the test. The deflection of each specimen and its development law during the test is shown in Figure 7. It can be seen that the PC specimens had the largest deflection during the test, and the SFRC specimens had a higher ultimate load and smaller deflection. After the end of the test, the deflection of the SFRC30-3 specimen did not exceed 9 mm, and the deflection of each measuring point was 34.6%, 47.6%, 52.03%, 55.0%, and 37.3% of that of the PC specimen, respectively (see Figure 7). The average deflections of the SFRC20-7 and SFRC40-5 specimens were 76.9% and 57.2%, respectively, of those of the PC specimen at the final loading stage. It is important to note that steel fiber can significantly improve the ductility of concrete, so that it has less deflection when it reaches the ultimate limit state, and effectively reduces brittle damage. Among the specimens, the ductility of SFRC was highest when the fiber content was 30 kg/m³, while the improvement in the ductility of SFRC40 was better than that of SFRC20, which is mainly due to the difference in content.

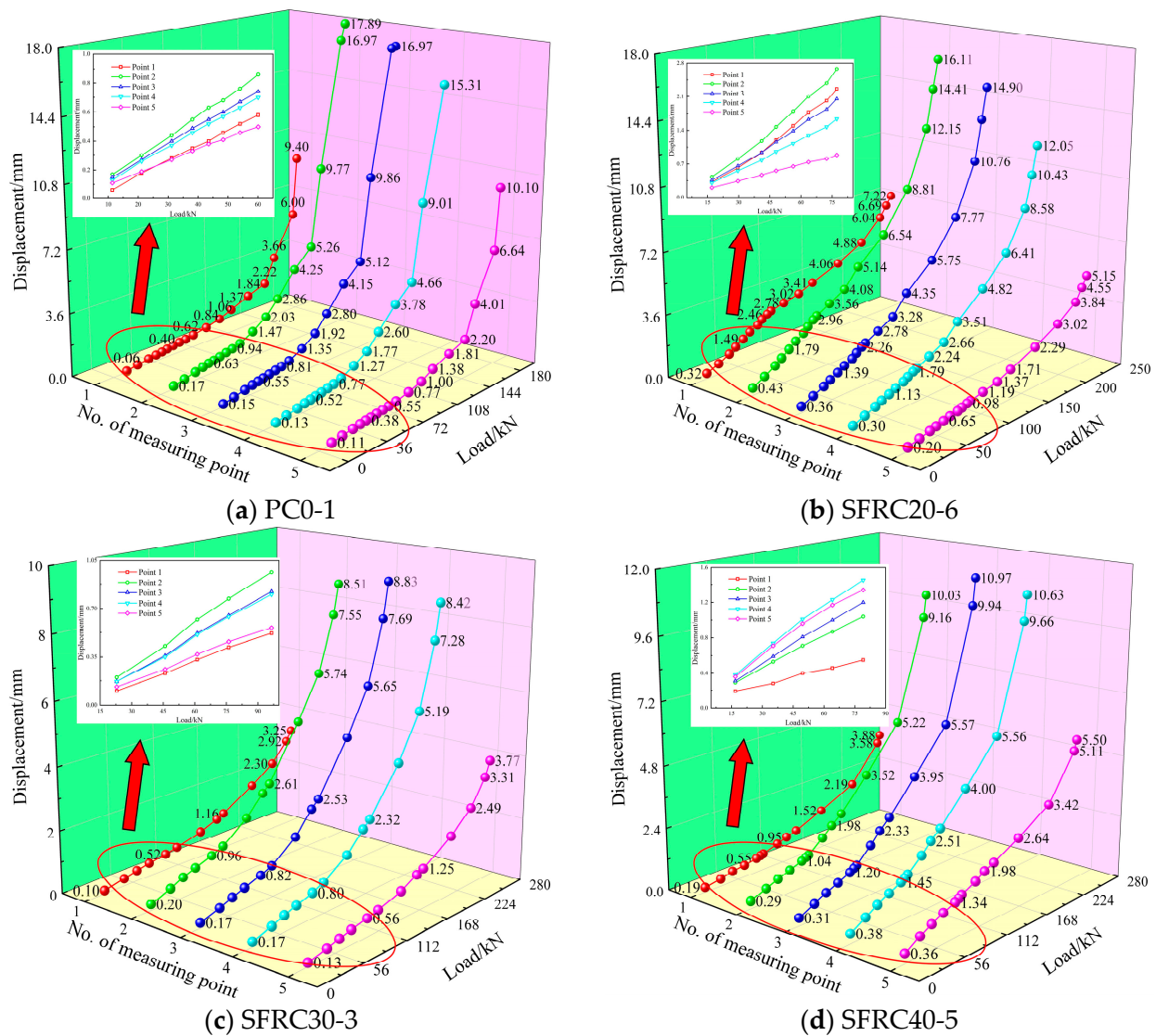


Figure 7. The displacement of PC and SFRC specimens.

By taking the displacement at measurement point 3 as the deflection of the specimen under a specific load, the change in deflection of the concrete before cracking was further investigated. The load–deflection curves before cracking were analyzed for PC specimens and SFRC with different fiber contents, and show that there is a highly linear relationship between them; the load–deflection curves of each specimen before cracking were fitted, and the results are shown in Figure 8. The fitting coefficient of each specimen is above 0.99, and the fitting effect is good. Slope F of the fitting curve represents the deflection of the specimen under the unit load, that is, the flexibility of the specimen. As shown in Figure 8, the flexibility of SFRC30-4 was the smallest, indicating that it has the strongest ability to resist deformation. The flexibility of SFRC20-6 was 0.0361, while that of SFRC40-5 was 0.0172, which is 2.56 and 1.22 times that of the PC specimens, respectively. That is, when the content of steel fiber is too high or too low, it may weaken the ability of concrete to resist deformation before cracking, and the weakening effect of low content is more obvious.

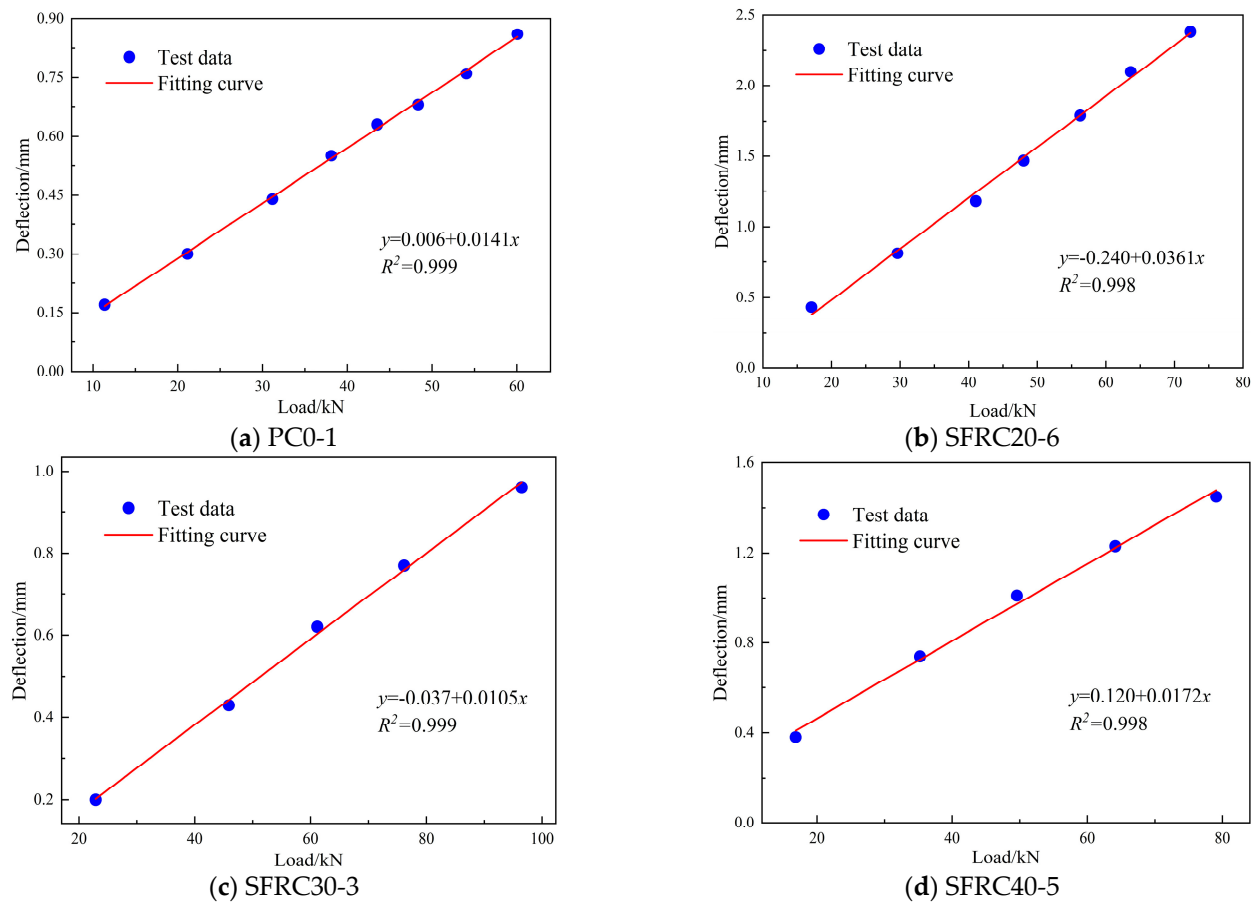


Figure 8. Fitting curves of the displacement of PC and SFRC specimens with the load.

3.3. The Prediction of Flexural Strength

3.3.1. The Cracking Load

Cracking load characterizes the crack resistance of concrete. According to the results in Section 3.2.1, the curve fitting for cracking load and the content of steel fiber was carried out. The fitting results are shown in Figure 9. Considering the steel fiber content commonly used in practical engineering, the fitting results mainly apply to the content range investigated in this study (20~40 kg/m³). When the steel fiber content is too high or too low, the cracking load of concrete may exhibit irregular variation. According to the derivation of Equation (2) (see Equation (3)), the optimal content of steel fiber for the cracking load is 31.19 kg/m³, and the corresponding maximum cracking load is 100.22 kN, which is 2.25 times that of PC. The most unfavorable content is 4.03 kg/m³, and the corresponding minimum cracking load is 40.11 kN, which is 0.90 times that of PC. As shown in Equation (2), when the steel fiber content is 0–8.51 kg/m³ and 44.32 kg/m³ or more, the cracking load of SFRC is lower than that of PC, and the steel fiber shows a negative effect on the crack resistance of the concrete. When the fiber content is 8.51–44.32 kg/m³, the cracking load of SFRC is higher than that of PC. At this time, steel fiber has a positive effect on crack resistance and toughening. This means that, in order to improve the crack resistance of concrete, the content of steel fiber should not be too low or too high. The addition of steel fiber can improve the crack resistance of concrete in most cases, and the crack resistance ability of concrete can be doubled by using the appropriate fiber content.

$$y = 44.472 - 2.263x + 0.317x^2 - 0.006x^3 \quad (2)$$

$$y = -2.263 + 0.634x - 0.018x^2 \quad (3)$$

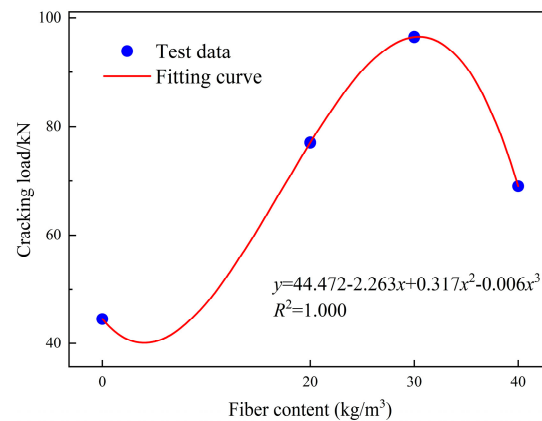


Figure 9. Fitting curves of the cracking load with the fiber content.

3.3.2. The Ultimate Load

The ultimate load characterizes the flexural capacity of the structure. In this test, the load corresponding to the crack width of 2.5 mm was taken as the ultimate load of SFRC. According to the results in Section 3.2.1, the ultimate load was fitted with fiber content. The fitting results are shown in Figure 10. Considering the steel fiber content commonly used in practical engineering, the fitting results mainly apply to the content range investigated in this study (20~40 kg/m³). When the steel fiber content is too high or too low, the ultimate load of concrete may exhibit irregular variation. According to the derivation of Equation (4) (see Equation (5)), the optimal fiber content of the ultimate load is 31.06 kg/m³, and the corresponding maximum flexural capacity of the structure is 253.25 kN, which is 1.39 times that of PC. The most unfavorable content is 4.86 kg/m³, and the corresponding minimum flexural capacity of the structure is 172.30 kN, which is 0.95 times that of PC. As shown in Equation 8, when the fiber content is 0–10.43 kg/m³ and above 43.46 kg/m³, the flexural capacity of SFRC is lower than that of PC, and the steel fiber has a negative effect on the flexural capacity of the concrete. When the fiber content is 10.43–43.46 kg/m³, the flexural capacity of SFRC is higher than that of PC, and the steel fiber can effectively improve the flexural performance of the structure. This means that, in order to improve the flexural performance of concrete, the steel fiber content should not be too low or too high. The addition of steel fiber can improve the flexural capacity of concrete in most cases, and the use of the appropriate fiber content can effectively improve the flexural performance of concrete.

$$y = 181.7 - 4.078x + 0.485x^2 - 0.009x^3 \quad (4)$$

$$y = -4.078 + 0.970x - 0.027x^2 \quad (5)$$

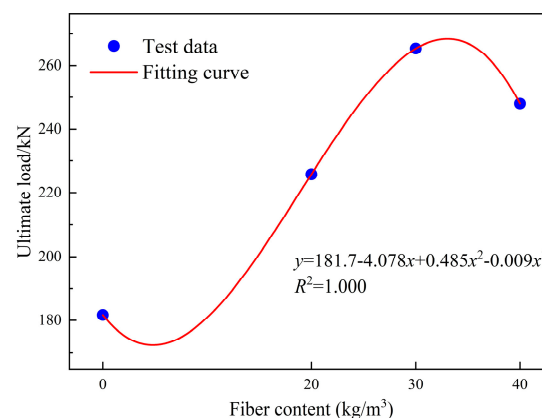


Figure 10. Fitting curves of the ultimate load with the fiber content.

3.4. The Optimum Content of Steel Fiber

For different mixture proportions and fiber materials, the mechanical properties of fiber reinforced concrete will also be different. In view of the mixture proportions (see Table 1) and steel fiber type used in this test, it has been concluded that the optimal steel fiber content, corresponding to the crack resistance and flexural capacity of concrete, is 31.19 kg/m^3 and 31.06 kg/m^3 . It is not difficult to see that the optimal content of steel fiber for flexural properties is 31 kg/m^3 , the corresponding cracking load is 100.21 kN, while the ultimate load is 253.25 kN, which is 125.34% and 39.38% higher than that of PC. At the same time, it is important to note that steel fiber has the most significant effect on the crack resistance of the structure. The flexural strength of SFRC is highly dependent on the change of steel fiber content.

4. The Discrete Element Simulation of SFRC

Through the experimental four-point bending test, the loading capacity and failure mode of SFRC were investigated. However, the enhancement mechanism and mesoscopic failure behaviors cannot be observed clearly. The failure mechanism of steel fiber is of great significance to the investigation of SFRC, and the finite element analysis cannot well reflect the enhancement process of steel fiber. Therefore, a refined model of SFRC is established in this paper, using the discrete element method, which shows high relevance to the experimental bending test. The mesoscopic mechanical properties of SFRC are investigated below.

4.1. Establishment of the Refined Model for SFRC

4.1.1. The Steel Fiber

The type of steel fiber used in this experiment was Dramix 4D 80/60 BG, and the structure diagram is shown in Figure 11a. In PFC2D, which is a discrete element particle flow piece of software, the shape of various objects can be created using a ‘clump template’, and the template constructed according to the actual shape and size of steel fiber. The template is used to generate a specified content of steel fiber, and the fibers are converted from clumps to balls. The simulation adopts the parallel bond contact model, which can well reflect the contact relationship between steel fiber and the concrete matrix. The mesoscopic parameters of the steel fiber balls are determined by calibrating the tensile strength of the steel fiber.

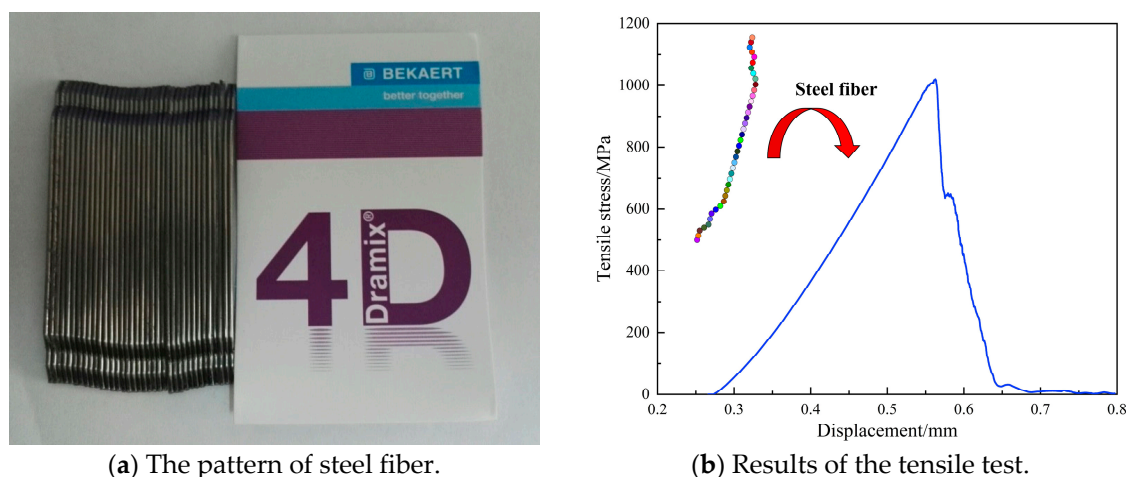


Figure 11. The numerical model of steel fiber.

The calibration results are shown in Figure 11b, where the tensile strength of the steel fiber model has reached more than 1000 MPa, consistent with the actual situation. The mesoscopic parameters of the steel fiber model are shown in Table 3.

Table 3. The mesoscopic parameters of steel fiber.

Parameters	Value
Contact bond modulus/GPa	300
Parallel bond modulus/GPa	10
Kratio	1.5
Parallel bond tensile strength/MPa	10,000
Parallel bond cohesion/MPa	1.3
Parallel bond friction angle/°	45
Friction coefficient	0.6

4.1.2. The Compressive Strength

In Section 3.1 of this paper, the rebound strengths of PC and SFRC were obtained via the rebound strength test, and the corresponding converted compressive strengths were obtained. Based on this, a numerical simulation of the cube compressive strength test was carried out via PFC2D (see Figure 12). As shown in Figure 12, the little red balls are steel fibers, and grey balls are the concrete matrix. Python was used to automatically adjust the mesoscopic parameters during calibration, and the fiber content was adjusted by changing the porosity of the steel fiber balls. The compressive strengths of the SFRC cube model with different fiber contents are shown in Figure 13 and Table 4, and its corresponding mesoscopic parameters are shown in Table 5.

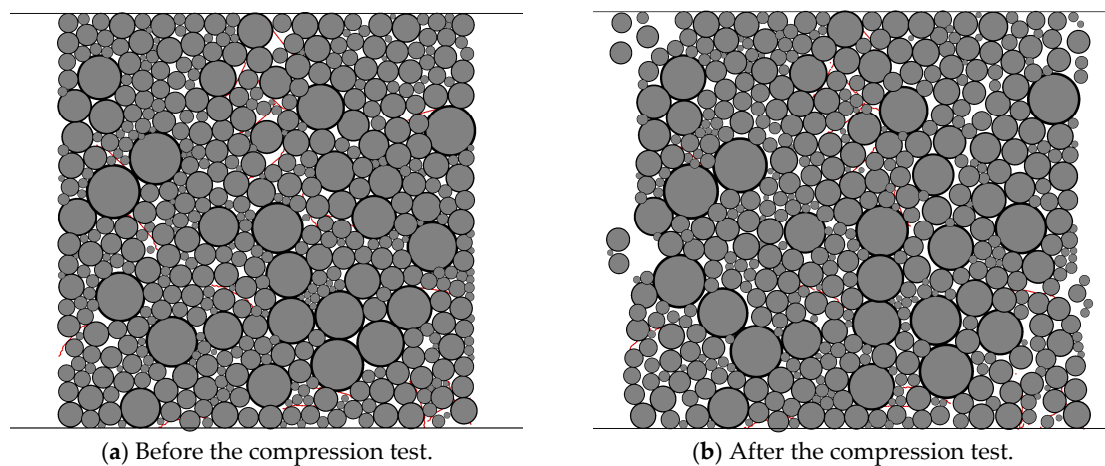
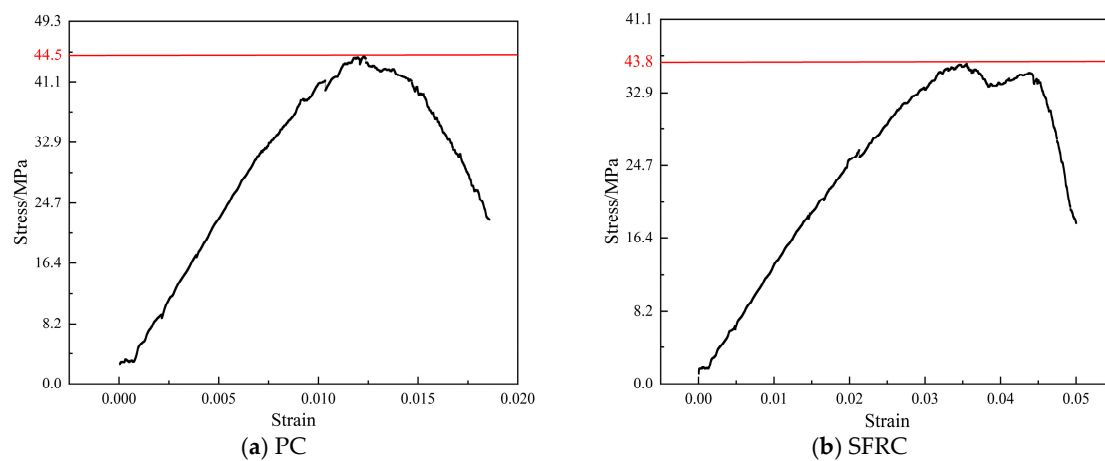
**Figure 12.** Process of numerical compression test on SFRC cube model.**Figure 13.** Stress–strain curves of PC and SFRC models.

Table 4. The calibration results for compressive strength.

Fiber Content (kg/m ³)	Experimental Compressive Strength/MPa	Numerical Compressive Strength/MPa	Error Rate/%
0	44.3	44.5	0.45
20	44.9	45.3	0.89
30	59.5	58.9	1.01
40	43.8	43.8	0.00

Table 5. The mesoscopic parameters of PC and SFRC with different fiber contents.

Parameters	Value			
	PC	SFRC20	SFRC30	SFRC40
Contact bond modulus/GPa			2.0	
Parallel bond modulus/GPa			0.1	
Kratio			2.0	
Parallel bond tensile strength/MPa			16.1	
Parallel bond cohesion/MPa			48.3	
Parallel bond friction angle/°			56	
Friction coefficient			0.6	
Porosity of concrete			0.1	
Porosity of SF	0	0.99744	0.99615	0.99487

4.1.3. The Results of the Screening Test

For the refined numerical analysis, it is important to establish the model according to the actual gradation of the concrete aggregate. The screening test was carried out to obtain the particle gradation of PC and SFRC beams. The screening results are shown in Tables 6 and 7, which provide a basis for establishing a refined numerical model with real particle gradation. As shown in Table 7, the smaller stones in the coarse aggregate (diameter: 5~10 mm) are named ‘Aggregate 1’, while the bigger stones (diameter: 10~20 mm) are named ‘Aggregate 2’. While casting specimens, the mixing rate of Aggregate 1 and Aggregate 2 was 3:7.

Table 6. The screening results of fine aggregate.

Aperture (mm)	4.75	2.36	1.18	0.6	0.3	0.15	<0.15
Results (g)	10	93	70	110	102	42	73
	2.0%	18.6%	14.0%	22.0%	20.4%	8.4%	14.6%

Table 7. The screening results of coarse aggregate (Aggregate 1–Aggregate 2 = 3:7).

Aperture (mm)	26.5	19.0	16.0	9.5	4.75	2.36	<2.36
Results (g)	0	88	208	2374	2663	905	254
	0.0%	1.4%	3.2%	36.5%	41.0%	13.9%	3.9%

Note: The smaller stones in the coarse aggregate (diameter: 5~10 mm) are named ‘Aggregate 1’, while the bigger stones (diameter: 10~20 mm) are named ‘Aggregate 2’.

4.2. The Meso-Mechanical Properties of SFRC

4.2.1. The Development of Microcracks

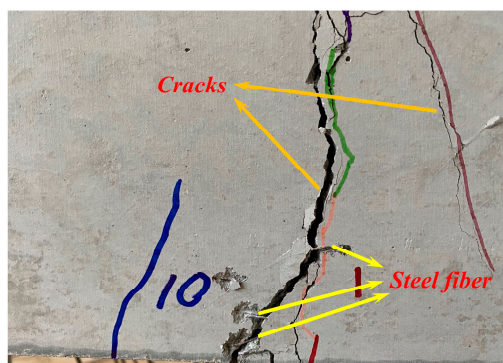
For the PC model, the initial crack appears at a load of 60 kN, under the loading point, which is consistent with the test results. After a period of time, no new cracks appear, and the main crack does not develop significantly. When the load reaches 80 kN, the crack

begins to develop. When the load reaches 100 kN, the main crack develops faster, but it is still not highly developed. New cracks appear under the middle of the span and right loading points, and the spacing between adjacent cracks is almost equal. When the load reaches 120 kN, the main crack under the left loading point suddenly develops violently, and the deflection of the model increases sharply. When the load reaches 130 kN, the crack width under the left loading point reaches 5.00 mm. At the same time, the load decreases sharply, the deflection continues to increase, and the model is damaged.

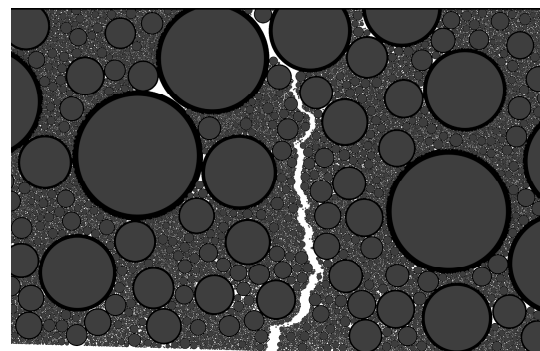
When steel fibers are added, such as in the SFRC40 model, the initial crack appears at a load of 70 kN, under the loading point, which is consistent with the experimental results. After a period of time, no new cracks appear, and the main cracks do not develop significantly. When the load reaches 80 kN, the cracks begin to develop. When the load reaches 100 kN, the development speed of cracks is accelerated. When the load reaches 220 kN, the crack width under the loading point reaches 1.80 mm, and new cracks appear under the left loading point and the middle of the span. When the load reaches 250 kN, the crack width under the right loading point reaches 5.00 mm, and the model is damaged.

In the process of loading, the change in crack width can well reflect the evolution law of cracks in the indoor bending test, but the number of cracks in the model is fewer than that of the indoor test. The main reason is that the transmission of load in the model requires a long balance time. Due to the limitation of computing power, the local force that may produce microcracks is not fully balanced and the next level of the load is started, which accelerates the development of main cracks and leads to stress redistribution, which suppresses the generation of new cracks.

When compared with the indoor four-point bending test, the cracking load of the PC model is 0.91 times that of the indoor test, and the ultimate load is 0.73 times. The indoor test specimens and numerical models of PC have cracks with uniform spacing, and the number of cracks is smaller than that of SFRC specimens and models. It can be seen from the numerical model that, when coarse aggregate particles appear in the crack development path of concrete, the path often changes, develops along the edge of coarse aggregate particles, and even bifurcates in the later stage of loading. There is only one highly developed crack in the PC model, and the development of the remaining cracks is not obvious, while the SFRC model has two highly developed cracks, but the height of crack development is lower than that of the PC model, which shows cracks about to develop at the top of the beam (see Figure 14). The cracks in the PC model develop rapidly and in a short time at a later stage, with a sudden increase in deflection and a sharp decrease in load, which belongs to brittle failure. The SFRC model has stable crack development, and there is no sudden increase in deflection when it is damaged, reflecting better ductility. The main crack in the PC model almost develops straight, while the crack development path in the SFRC model is tortuous. These results are highly consistent with the indoor test results, indicating that the numerical model can well reflect the crack development law of PC and SFRC.



(a) Major crack on SFRC specimen.



(b) Major crack on SFRC model.

Figure 14. Major crack patterns on the surfaces of SFRC specimen and model.

4.2.2. The Force Chain Network

The analysis of the research results shows that the granular materials of concrete are usually densely distributed, and the contact between adjacent particles forms a path to transmit loads. The propagation path of force is called the force chain. Several force chains are connected to each other to form a network throughout the structure, transmitting the weight of the structure and bearing loads. The complex dynamic response of the force chain network determines the macroscopic mechanical properties of the system, which is the basic force form of the structure. In order to quantify the strength of the force chain, relevant researchers have proposed several methods. In this paper, according to the average value of contact force \bar{F} [31], the strong force chain is defined as $F > \bar{F}$, the middle force chain is defined as $\bar{F} > F > 0.5\bar{F}$, and the weak force chain is defined as $F < 0.5\bar{F}$. There is a great correlation between the dynamic stress characteristics and the static accumulation properties of particles and the development law of the meso-scale force chain. There is a great correlation between the macroscopic mechanical properties of structure and the development law of the mesoscopic force chain.

Figure 15a,c,e show the force chain network of PC specimens in each stage of the test. The thicker the force chain, the greater the contact force between the particles. In Figure 15, the red line represents the compressive force chain, and the yellow line represents the tensile force chain. It can be seen that, in the initial loading stage of the test, the force chain first spreads from the loading points and the supports, and then spreads to all parts of the structure. At this time, the height of the compressive force chain is about $1/4$ of the height of the specimen (h), the height of the tensile force chain is about $1/2 h$, and there is a weak area of the force chain in the middle of the model. In the middle stage of loading, the force chain near the loading points mainly propagates in the horizontal direction, and more strong horizontal force chains are generated in the compression zone and the tension zone. The force chain network is gradually dense and tends to be stable, and the height of the weak force chain zone in the middle of the model is reduced (see Figure 16). The load transfer on both sides of the model is mainly completed by the contact and compression of particles at the top of the middle span.

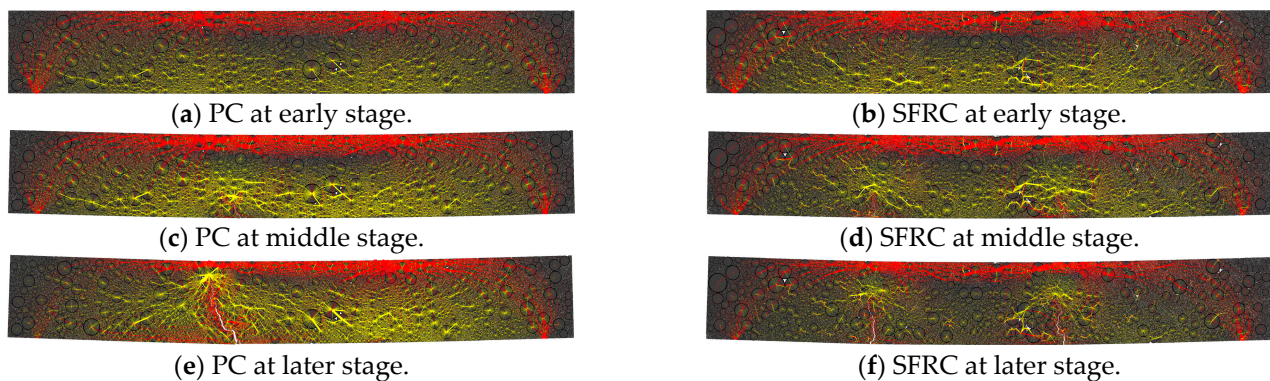
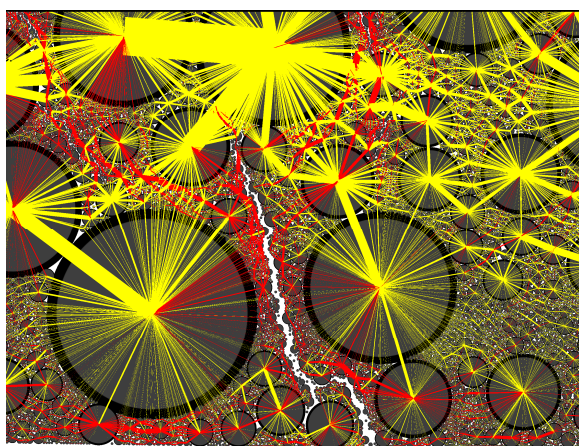
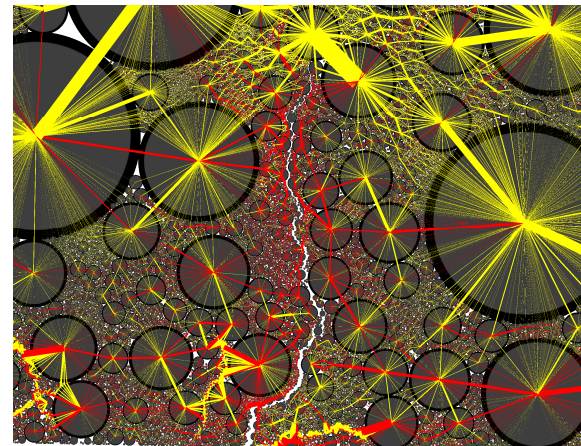


Figure 15. The force chain network of PC and SFRC models at different loading stages.

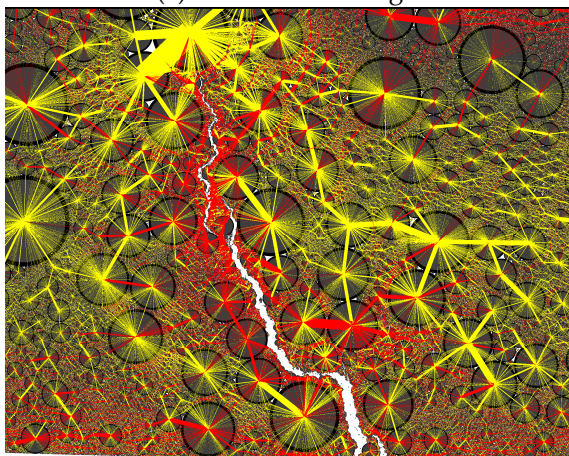
The force chain network of the PC model at the later stage of loading is shown in Figure 17e. The force chains at the top of the model continue to develop, and the force chain network has stabilized. The force chain network at the bottom of the model is also gradually dense. At this time, a crack appears under the left loading point. The tensile force chains there have been broken, while the compressive force chains are mainly near the edge of the crack. The directions of these compressive force chains are mainly along the direction of crack development. This is due to the continuous deformation of the crack during the development, which leads to the mutual extrusion of the edge particles. There are strong tensile force chains at the top of crack, which shows stress concentration. When the stress continues to increase until it exceeds the ultimate strength of the material, the crack will expand sharply, eventually leading to structure instability.



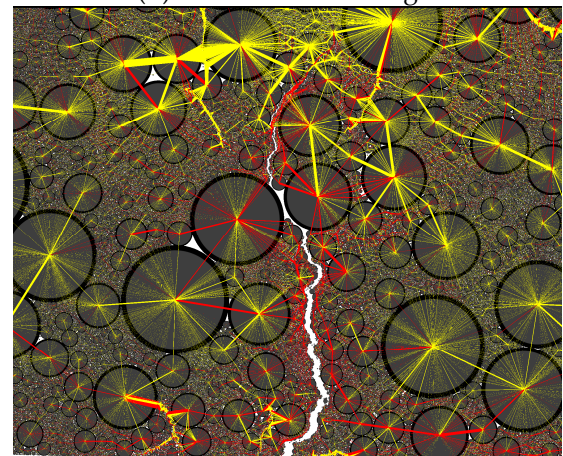
(a) PC at middle stage.



(b) SFRC at middle stage.

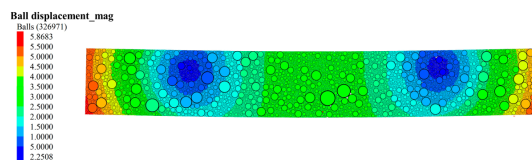


(c) PC at later stage.

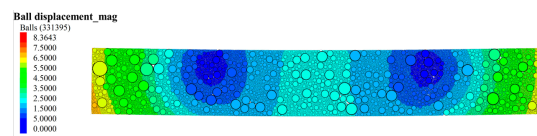


(d) SFRC at later stage.

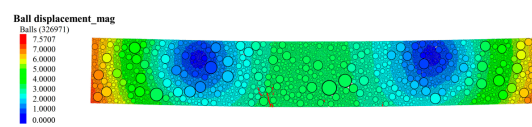
Figure 16. The local force chain network diagrams of PC and SFRC models at different loading stages.



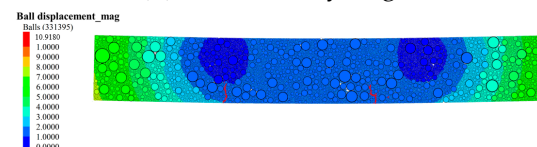
(a) PC at early stage.



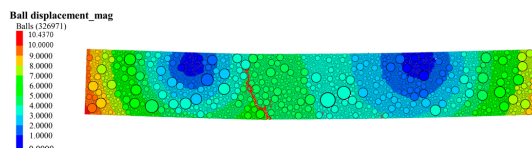
(b) SFRC at early stage.



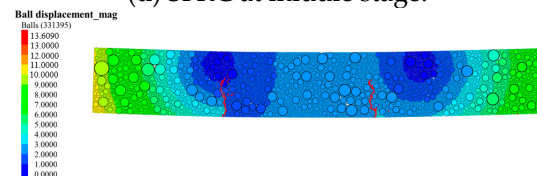
(c) PC at middle stage.



(d) SFRC at middle stage.



(e) PC at later stage.



(f) SFRC at later stage.

Figure 17. The displacement ($\times 10^{-3}$ m) nephogram of PC and SFRC models at different loading stages.

Figure 15b,d,f show the force chain distribution of the SFRC model at each stage. The development process of the force chains is basically the same as that of the PC model.

When cracks occur, both sides of the crack are compressive force chains, and there are concentrated strong tensile force chains at the top of cracks. Different from the PC model, strong force chains not only appear between the coarse aggregate particles, but also exist near most of the steel fibers. When the height of a crack develops at the later stage, the tensile force chains between concrete particles in the SFRC model are significantly weaker than in the PC model, as the steel fiber bears most of the tensile stress, thus significantly improving the bearing capacity of the model.

In this sense, the development of the force chain network allows for analysis of the macroscopic test results from the microscopic point of view, thus providing a certain analytical basis for the study of the flexural mechanical properties of SFRC.

4.2.3. The Displacement Nephogram

In all mechanical properties, the displacement of the structure is very important when studying the failure mode and microscopic mechanism of specimens. As the test progresses, the displacement of each part of the specimen continues to develop [32,33]. Figure 17 shows the displacement nephograms of the PC and SFRC40 models at each stage of the test.

At the beginning of the test, the displacement first appears under the two loading points, and diffuses to the lower part of the specimen in a trapezoid shape. Then, the displacement at loading points increases continuously and diffuses along the path. After the first loading stage, the displacement of the model is balanced and, finally, two ringed low displacement zones appear outside the two loading points. The displacement near the center of the zone is the smallest, and the displacement at the edges of both sides of the model is the largest. The ringed low displacement zone of the PC model is smaller than that of the SFRC model, and the displacement of the SFRC model is smaller. In the middle stage of the test, the center of the ringed low displacement zone on both sides shifts to the inside of the model, and the top of the left main crack on the SFRC model is close to the low displacement zone. Obviously, the displacement inside the two loading points of the SFRC model is more uniform and stable than that of the PC model, while the displacement of the PC model shows gradient distribution, which may lead to stress and strain concentration. When the crack develops higher, the center of the low displacement zone begins to shift upward. The range of the zone on the PC model is significantly smaller than that on the SFRC model. The displacement distribution of the SFRC model begins to change. The crack blocks the transmission of displacement on both sides. The displacement of the particles near the middle-span side of the two cracks decreases. At the same time, the particles near both sides of the model continue to move outward. These changes further promote the development of cracks, so that the displacement difference on both sides of the cracks increases.

4.3. The Crack Resistance Mechanism of Steel Fiber

The abovementioned simulation results explain why, when a new crack appears near the outside of the main crack in the experimental bending test, the smaller the distance between the two cracks, the more the new crack inhibits the development of the main crack. Combined with the results of the displacement nephograms and the distribution of the force chain network, these results can be analyzed to understand that the generation of new cracks dissipates the strain energy on one side of the main crack, which blocks the transmission of force and displacement, thus inhibiting the development of the main crack. SFRC produces more small cracks than ordinary plain concrete, which accelerates the energy dissipation near the main crack, reflecting the crack resistance of steel fiber.

From the development of the force chain network, it can be seen that the steel fibers in the tension zone are mostly near the strong force chains, which bear most of the tensile stress. It can be seen from Figure 17 that the cracks mainly appear in the tensile weak area where the steel fiber is vertically distributed. At this time, the vertical steel fibers inhibit the extrusion effect between the particles on both sides, that is, inhibit the transmission of force and displacement, thus changing the development direction of the cracks. At the

same time, the bridging effect of horizontal fibers can effectively inhibit the development of cracks. When the crack develops, both sides of the crack are compressive force chains, and there are strong tensile force chains on the top of crack. When the structure cracks, the tensile capacity of the concrete matrix fails, and the load is all borne by the nearby steel fibers and transferred to the other end where new cracks form. This leads to stress redistribution, and then a series of cracks appear.

5. Conclusions and Future Work

Based on our investigations, the following conclusions can be drawn.

- (1) The steel fiber in question (Dramix 4D 80/60 BG) can improve the compressive strength of concrete. The compressive strength of SFRC20 and SFRC30 was increased by 1.3% and 34.3%, respectively, while that of SFRC40 decreased by 1.3%, indicating that too much steel fiber has a negative effect on the compressive strength of concrete.
- (2) The cracks on SFRC are subtler, more numerous, and widely distributed under the bending load, but the cracks on PC are highly developed. The cracking loads of SFRC20, SFRC30, and SFRC40 were increased by 34.57%, 90.48%, and 24.87%, respectively, which shows the significant effect of steel fibers on the crack resistance of concrete. The optimal fiber content for the cracking capacity of SFRC was 31.19 kg/m³. The ultimate load of SFRC20, SFRC30, and SFRC40 was increased by 28.12%, 47.22%, and 40.59%, respectively, suggesting that steel fiber effectively improves the flexural capacity of concrete. The optimal fiber content for the flexural performance of SFRC was 31.06 kg/m³.
- (3) The refined discrete element numerical model for SFRC beams was obtained. The numerical results were compared with the experimental results, showing good agreement. The DEM models established using PFC2D could simulate the failure process of the beams. The crack first appears at the place where the contact is weak, the edge of the crack is full of compressive force chains, and the tensile force chains are concentrated at the top of the crack. With the development of the crack, the horizontal displacement difference between the left and right sides of the crack becomes larger and larger, which accelerates the development of the crack width.
- (4) The crack resistance mechanism of steel fiber is that the horizontally distributed steel fiber bridges both sides of the crack to inhibit crack development. In addition, the vertically distributed steel fiber guides the crack to the large particles with strong contact force by changing the development direction of the crack, thus inhibiting crack height development in the later stage. The numerical results explained the phenomenon of the macroscopic test from a microscopic scale.

Finally, the integrated experimental and discrete element numerical methodology was demonstrated as being able to translate the results obtained from the experimental four-point bending tests to DEM models. For future research, the application of this methodology is suggested for predicting the behavior of SFRC structural members. The bonding force between the steel fibers and the matrix is the key factor for preventing matrix crack propagation. For these cases, it is extremely important to better reflect the bonding effect of steel fiber and the concrete matrix.

Author Contributions: Conceptualization, H.Z.; Methodology, J.W.; Software, N.H.; Validation, H.X.; Formal analysis, Z.W.; Investigation, X.R. All authors have read and agreed to the published version of the manuscript.

Funding: This research received no external funding.

Data Availability Statement: The original contributions presented in the study are included in the article, further inquiries can be directed to the corresponding author.

Conflicts of Interest: Authors Jian Wu and Nengfang He were employed by the company Road & Bridge South China Engineering Co., Ltd. The remaining authors declare that the research was

conducted in the absence of any commercial or financial relationships that could be construed as a potential conflict of interest.

References

1. Zhu, H.; Li, C.; Gao, D.; Yang, L.; Cheng, S. Study on mechanical properties and strength relation between cube and cylinder specimens of steel fiber reinforced concrete. *Adv. Mech. Eng.* **2019**, *11*, 4. [\[CrossRef\]](#)
2. Cao, Q.; Gao, Q.; Jia, J.; Gao, R. Early-Age Cracking Resistance of Fiber-Reinforced Expansive Self-Consolidating Concrete. *ACI Mater. J.* **2019**, *116*, 15–26. [\[CrossRef\]](#)
3. Bolat, H.; Simsek, O. Evaluation of Energy Absorption of Macro Synthetic and Steel Fiber Reinforced Concretes. *Rev. Rom. Mater.* **2015**, *45*, 123–132.
4. Nili, M.; Afroughsabet, V. Combined effect of silica fume and steel fibers on the impact resistance and mechanical properties of concrete. *Int. J. Impact Eng.* **2010**, *37*, 879–886. [\[CrossRef\]](#)
5. Xu, S.; Lyu, Y.; Xu, S.; Li, Q. Enhancing the initial cracking fracture toughness of steel-polyvinyl alcohol hybrid fibers ultra high toughness cementitious composites by incorporating multi-walled carbon nanotubes. *Constr. Build. Mater.* **2018**, *195*, 269–282. [\[CrossRef\]](#)
6. ACI 544.1 R-96; State-of-the-Art Report on Fiber Reinforced Concrete. American Concrete Institute: Farmington Hills, MI, USA, 1996.
7. Thomas, J.; Ramaswamy, A. Mechanical Properties of Steel Fiber-Reinforced Concrete. *J. Mater. Civ. Eng.* **2007**, *19*, 385–392. [\[CrossRef\]](#)
8. Tadepalli, P.R.; Mo, Y.L.; Hsu, T.T.C. Mechanical properties of steel fibre concrete. *Mag. Concr. Res.* **2013**, *65*, 462–474. [\[CrossRef\]](#)
9. Köksal, F.; Şahin, Y.; Gencel, O.; Yiğit, I. Fracture energy-based optimisation of steel fibre reinforced concretes. *Eng. Fract. Mech.* **2013**, *107*, 29–37. [\[CrossRef\]](#)
10. Ma, K.; Ma, Y.; Liu, B. Experimental investigation on ultra high performance fiber reinforced concrete beams. *Mech. Adv. Mater. Struct.* **2022**, *30*, 1155–1171. [\[CrossRef\]](#)
11. Zhang, J.; Yan, C.W.; Jia, J.Q. Compressive Strength and Splitting Tensile Strength of Steel Fiber Reinforced Ultra High Strength Concrete (SFRC). *Appl. Mech. Mater.* **2010**, *34–35*, 1441–1444. [\[CrossRef\]](#)
12. Doyon-Barbant, J.; Charron, J.-P. Impact of fibre orientation on tensile, bending and shear behaviors of a steel fibre reinforced concrete. *Mater. Struct.* **2018**, *51*, 157. [\[CrossRef\]](#)
13. Varona, F.; Baeza, F.; Bru, D.; Ivorra, S. Evolution of the bond strength between reinforcing steel and fibre reinforced concrete after high temperature exposure. *Constr. Build. Mater.* **2018**, *176*, 359–370. [\[CrossRef\]](#)
14. Chu, S.; Kwan, A. A new bond model for reinforcing bars in steel fibre reinforced concrete. *Cem. Concr. Compos.* **2019**, *104*, 103405. [\[CrossRef\]](#)
15. Bošnjak, J.; Sharma, A.; Grauf, K. Mechanical Properties of Concrete with Steel and Polypropylene Fibres at Elevated Temperatures. *Fibers* **2019**, *7*, 9. [\[CrossRef\]](#)
16. Awolusi, T.; Oke, O.; Akinkulore, O.; Sojobi, A. Application of response surface methodology: Predicting and optimizing the properties of concrete containing steel fibre extracted from waste tires with limestone powder as filler. *Case Stud. Constr. Mater.* **2018**, *10*, e00212. [\[CrossRef\]](#)
17. Baby, F.; Marchand, P.; Toutlemonde, F. Shear Behavior of Ultrahigh Performance Fiber-Reinforced Concrete Beams. I Experimental Investigation. *J. Struct. Eng.* **2014**, *140*, 5. [\[CrossRef\]](#)
18. Magureanu, C.; Sosa, I.; Negrutiu, C.; Heghes, B. Bending and shear behavior of ultra-high performance fiber reinforced concrete. *High Perform. Struct. Mater.* **2010**, *112*, 79–89.
19. Singh, M.; Sheikh, A.; Ali, M.M.; Visintin, P.; Griffith, M. Experimental and numerical study of the flexural behaviour of ultra-high performance fibre reinforced concrete beams. *Constr. Build. Mater.* **2017**, *138*, 12–25. [\[CrossRef\]](#)
20. Zagon, R.; Zoltan, K. Shear Behaviour of UHPC Concrete Beams. *Procedia Technol.* **2016**, *22*, 122–126. [\[CrossRef\]](#)
21. Xia, J.; Xiao, Y.; Mackie, K.R.; Al-Ramahee, M.; Mirmiran, A. Dowel action and shear strength contribution of high strength rebar embedded in ultra-high performance fiber reinforced concrete. *Eng. Struct.* **2015**, *83*, 223–232. [\[CrossRef\]](#)
22. Khalil, W.I.; Tayfur, Y.R. Flexural strength of fibrous ultra high performance reinforced concrete beams. *ARP J. Eng. Appl. Sci.* **2013**, *8*, 200–214. [\[CrossRef\]](#)
23. Yang, I.H.; Joh, C.; Kim, B.-S. Structural behavior of ultra high performance concrete beams subjected to bending. *Eng. Struct.* **2010**, *32*, 3478–3487. [\[CrossRef\]](#)
24. Kan, W.; Yang, Z.; Yin, W. Simulation of Four-Point Bending Fracture Test of Steel-Fiber-Reinforced Concrete. *Materials* **2022**, *15*, 7146. [\[CrossRef\]](#) [\[PubMed\]](#)
25. Kusumaningrum, P.; Budiono, B.; Fajar, M. Elitha XFEM based fracture analysis of single notch reactive powder concrete specimen subjected to three point bending test. *E3S Web Conf.* **2020**, *156*, 05027. [\[CrossRef\]](#)
26. Soetens, T.; Matthys, S.; Taerwe, L.; Gysel, A. Basis of a Finite-Element Simulation Tool to Predict the Flexural Behavior of SFRC Prisms. *High Perform. Fiber Reinf. Cem. Compos.* **2012**, *2*, 91–98. [\[CrossRef\]](#)
27. Qsymah, A.; Sharma, R.; Yang, Z.; Margetts, L.; Mummery, P. Micro X-ray computed tomography image-based two-scale homogenisation of ultra high performance fibre reinforced concrete. *Constr. Build. Mater.* **2017**, *130*, 230–240. [\[CrossRef\]](#)

28. Ren, W.; Yang, Z.; Sharma, R.; Zhang, C.; Withers, P.J. Two-dimensional X-ray CT image based meso-scale fracture modelling of concrete. *Eng. Fract. Mech.* **2015**, *133*, 24–39. [[CrossRef](#)]
29. Sun, B.; Wang, X.; Li, Z. Meso-scale image-based modeling of reinforced concrete and adaptive multi-scale analyses on damage evolution in concrete structures. *Comput. Mater. Sci.* **2015**, *110*, 39–53. [[CrossRef](#)]
30. Sliseris, J. Numerical analysis of reinforced concrete structures with oriented steel fibers and re-bars. *Eng. Fract. Mech.* **2018**, *194*, 337–349. [[CrossRef](#)]
31. Cundall, P.A. A discontinuous future for numerical modelling in geomechanics? *Proc. Inst. Civ. Eng.—Geotech. Eng.* **2001**, *149*, 41–47. [[CrossRef](#)]
32. Gong, L.; Nie, L.; Liu, C.; Xu, Y. Modelling Triaxial Tests on Fibre-Reinforced Sands with Different Fibre Orientations Using the Discrete Element Method. *KSCE J. Civ. Eng.* **2020**, *24*, 2268–2280. [[CrossRef](#)]
33. Wang, C.; Deng, A.; Taheri, A. Three-dimensional discrete element modeling of direct shear test for granular rubber-sand. *Comput. Geotech.* **2018**, *97*, 204–216. [[CrossRef](#)]

Disclaimer/Publisher’s Note: The statements, opinions and data contained in all publications are solely those of the individual author(s) and contributor(s) and not of MDPI and/or the editor(s). MDPI and/or the editor(s) disclaim responsibility for any injury to people or property resulting from any ideas, methods, instructions or products referred to in the content.